energies

MDPI

Article

Numerical Modeling on Dissociation and Transportation of Natural Gas Hydrate Considering the Effects of the Geo-Stress

Rui Song [1,2,3], Yaojiang Duan [1,*], Jianjun Liu [2,3,*] and Yujia Song [2,3]

[1] School of Geoscience and Technology, Southwest Petroleum University, Chengdu 610500, China
[2] State Key Laboratory of Geomechanics and Geotechnical Engineering, Institute of Rock and Soil Mechanics, Chinese Academy of Sciences, Wuhan 430071, China
[3] University of Chinese Academy of Sciences, Beijing 100049, China
* Correspondence: duanyaojiangswpu@163.com (Y.D.); jjliu@whrsm.ac.cn (J.L.)

Abstract: A deep understanding of the dissociation and transportation mechanism of natural gas hydrate (NGH), taking into account the effects of geo-stress, contributes to optimizing the development strategy and increases the exploitation efficiency of NGH. In this paper, the mathematical model, coupled with fluid heat and mass transfer, multiphase flow mechanics, and reaction kinetics with phase change in the process of hydrate decomposition was established. An axisymmetric two-dimensional model was developed to simulate the depressurization decomposition process of natural gas hydrate in the Berea sandstones. FLUENT software was used to solve the fundamental governing equations of the multi-phase flow, and UDF programming was employed to program the hydrate decomposition model and the modified permeability model in the dissociation and transportation of NGH. The simulation results were then validated by Masuda's experimental data. The effects of gas saturation, outlet pressure, temperature, absolute permeability and geo-stress on the decomposition of natural gas hydrate were studied. The results indicated that a higher absolute permeability, higher initial gas saturation, lower outlet pressure, and higher initial temperature advance the decomposition rate of hydrate. Thus, an optimized production plan is essential to promote the extraction efficiency of the NGH. The geo-stress causes a decrease in the porosity and permeability of the porous rock, which restricts the efficiency of the heat and mass transfer by the fluid flow, leading to a slower dissociation and transportation rate of the NGH. Thus, it is important to take geo-stress into consideration and balance the extracting efficiency and the well pressure, especially when the NGH is developed by depressurization.

Keywords: natural gas hydrate; heat and mass transfer; reaction kinetics; geo-stress

Citation: Song, R.; Duan, Y.; Liu, J.; Song, Y. Numerical Modeling on Dissociation and Transportation of Natural Gas Hydrate Considering the Effects of the Geo-Stress. *Energies* **2022**, *15*, 9311. https://doi.org/10.3390/en15249311

Academic Editor: Hossein Hamidi

Received: 28 October 2022
Accepted: 26 November 2022
Published: 8 December 2022

1. Introduction

The increasing global demands for energy and environmental protection urge governments and scientists to exploit unconventional oil and gas resources, but with tremendous reservation, such as coalbed methane, shale gas, tight sandstone gas, and natural gas hydrate, among others [1,2]. Natural gas hydrate (NGH), which accounts for the largest proportion of unconventional natural gas resources, is a kind of high-quality, efficient, and clean energy with great potential [3]. NGH is a non-fixed stoichiometric cage-like crystalline compound formed by the reaction of one or several small molecular gases with water at a certain temperature and pressure [4]. One cubic meter of NGH can release 164 cubic meters of methane in standard conditions, which is 10 times the energy density of other unconventional gas source rocks (such as coalbed methane), and 2~5 times the energy density of conventional natural gas [5]. Therefore, the commercial exploitation of NGH is crucial to worldwide energy supply and economic development.

NGH requires low temperature and high-pressure conditions to maintain a stable state, and is generally distributed in deep sea or continental permafrost. Up to now, the

short-term field tests of hydrate exploitation in the world have been carried out in sandy (or partially sandy) sediments [6]. The exploitation methods of NGH mainly include the thermal stimulation method, depressurization method, chemical reagent injection method and CO_2 replacement method [7–9]. Current thermal stimulation methods in mining technology are inefficient and can only achieve local heating [10]. The chemical reagents huff-n-puff method is high-cost and low-efficiency, and has a potential risk of environmental pollution [11]. The efficiency of the carbon dioxide replacement method is also low [12]. Consequently, the depressurization method is regarded as the most economical and environmentally friendly way for NGH exploitation [13–15]. By depressurization, the solid NGH decomposes into gas and water, and, then, gas escapes from the reservoir. Stable NGH serves as the cementing material for the mineral grains of rocks and improves the strength of the rock mass. The dissociation of the NGH may cause potential geo-hazards. Thus, a study on the dissociation and transportation mechanism of NGH, considering the effects of the geo-stress, contributes to the economic and safe development of NGH.

To date, extensive studies have been performed to investigate the dissociation and transportation process of NGH in porous media by numerical modeling. Zhao et al. [16] simulated the distribution of temperature, pressure, and hydrate saturation as natural gas hydrate decomposed in a two-dimensional axisymmetric model. Deng et al. [17] established a coupling model of two-phase flow and heat transfer for hydrate dissociation. Zhang et al. [18] adopted the dynamic grid algorithm to analyze the effects of permeability, lithology, and reservoir compression modulus on the recovery efficiency of natural gas hydrate in the core. Based on the implicit pressure–explicit saturation (IMPES) method, Liang et al. [19] created a two-dimensional axisymmetric model and analyzed the effects of outlet pressure, initial hydrate saturation and other parameters on hydrate decomposition and gas production rate in porous media. Ruan et al. [20] investigated the responses of hydrate dissociation to permeability and hydrate saturation of the reservoir. Two-dimensional axisymmetric models were established in FLUENT software to investigate the impact of temperature, permeability, pressure, phase distribution and other factors on the rate of NGH dissociation [21–28]. However, the geo-stress was not considered in these studies. The effective pressure is believed to be one of the key factors for efficiency and stability in the formation of NGH [29]. White et al. [30] integrated the geomechanical calculation into the existing thermal and hydrological coupling model framework to simulate the process of NGH exploitation by using IGHCCS2 codes. Cheng et al. [31] developed a gas–water two-phase fluid mechanics coupling model to investigate the effects of the interaction of the fluid and solid on the gas production of NGH. Lee et al. [32] developed a 3D geological model to investigate the geo-stress on gas production of NGH by using the cyclic depressurization method. Liu et al. [33] utilized the thermal-hydrological-mechanical-chemical (THCM) coupling model to study the geomechanical issues during the exploitation of NGH. Wu et al. [34] investigated the effects of the effective stresses on the permeability and porosity of natural gas hydrate reservoirs with different NGH saturations. Sun et al. [35] developed a fully coupled thermal-hydrological-mechanical-chemical (THCM) model. The impacts of compressibility on the rate of gas production, pore pressure, temperature, permeability, and other parameters were investigated. Jang et al. [36] studied the effects of geo-stress on fluid flow in NGH reservoirs. Kimoto et al. [37] conducted a numerical simulation based on a chemical-thermal-mechanical coupling model and an updated Lagrangian equation, and investigated the influencing factors of ground deformation caused by NGH dissociation. Sun et al. [38,39] used COMSOL to simulate the mechanical behavior of NGH by integrating the Mohr–Coulomb model into the fully coupled thermal-water-mechanics model. Cheng et al. [40] proposed a thermal-hydro-mechanical (THM) coupling model and studied the distribution of pressure, saturation of each phase, temperature, and mechanical parameters around the wellbore. Wan et al. [41] proposed a thermal-water-mechanical-chemical (THMC) coupling model based on the CVFEM framework, which was then validated by Masuda's triaxial compression experiment [42] and sandstone core experiment [43]. However, the mechanical parameters used in most of

these studies were estimated empirically, which limited the validation and applicability in engineering applications.

In this paper, a mathematical model, considering fluid heat and mass transfer, multiphase flow mechanics, and reaction kinetics with phase change in the process of hydrate decomposition, was established. In this model, the mechanical properties of the Berea sandstone and its stress sensitivity were adopted. The THMC codes were programmed in C language and used as a subroutine in FLUENT software. The Masuda's experiments on the Berea sandstone were simulated and used as benchmark data for model verification. The effects of initial gas saturation, outlet pressure, initial temperature, absolute permeability and geo-stress on the decomposition of natural gas hydrate were studied.

2. Methods

2.1. Computer Model

This work employed Masuda's experimental benchmark data [43] to validate the numerical model, and, on that basis, addressed and investigated the effect of effective stress on hydrate decomposition and gas production in sandy sediments. Masuda's experiment involved distributing a specified volume of water, methane gas, and hydrate in the core of a cylindrical sandstone. The core had a cross-sectional size of 20.3 cm^2. The gas phase followed the Peng–Robinson equations. The Euler model was adopted to simulate the multiphase flow in the porous rock containing NGH. This study turned the original three-dimensional model into a two-dimensional axisymmetric model for processing using ICEM software, as in Figure 1. The symmetry axis was chosen to be the bottom edge, and the calculation area was divided into 120 × 20 grids. FLUENT was then used to import the mesh model. In Masuda's experiment, the left side was the outlet, while the surrounding and right side were the non-slip and free convection walls with external heat flow through the rubber casing around the sandstone. In this study, the casing thickness in the experiment was 10 mm, and the appropriate range of h was 1.90–272.7 $W/(m^2 \cdot K)$, and 50 $W/(m^2 \cdot K)$ was employed. The temperature monitoring points were P1 (7.5, 2.5), P2 (15, 2.5), and P3 (22.5, 2.5) in Figure 1. The initial conditions, and boundary conditions used in this simulation followed the experiment of Masuda et al. [43], as shown in Table 1 The properties of the fluids in the simulation referred to the standard database at the same temperature and pressure conditions as the experiment. The material properties of the porous sandstone referred to average values of the Berea sandstones in literature [44], as shown in Table 2.

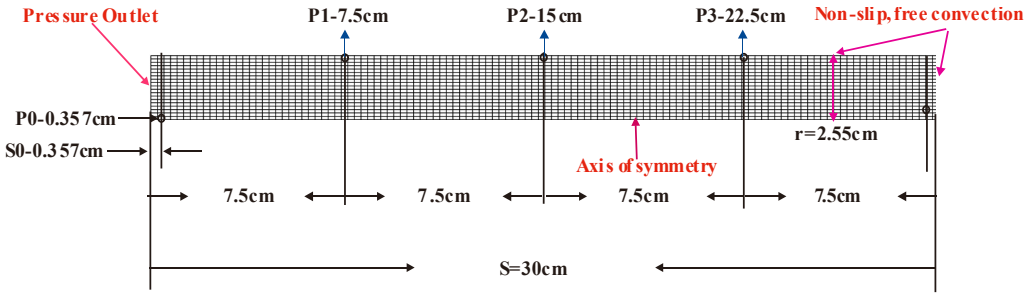

Figure 1. Mesh model and boundary conditions for Masuda's experiment.

Table 1. Initial conditions, boundary conditions and properties of sandstone cores in Masuda's experiment.

Properties	Value	Properties	Value
Average saturation of initial hydrate	0.501	Initial permeability of sandstone core	97.98 mD
Average saturation of initial water	0.199	Sandstone core porosity	0.182
Average saturation of initial methane gas	0.3	Joule-Thomson throttling coefficient	-1.5×10^{-4}
initial temperature	275.45 K	Critical pressure of methane	4.599 MPa
initial pressure	3.75 MPa	Critical temperature of methane	190.56 K
outlet pressure	2.84 MPa	ambient temperature	274.15 K

Table 2. Material properties in the simulation.

	Density (kg/m^3)	Fluid Viscosity (cP)	Thermal Conductivity ($w \cdot m^{-1} \cdot k^{-1}$)	Thermal Capacity ($J \cdot kg^{-1} \cdot k^{-1}$)
water	1001.5	1	0.6	4180
hydrate	913	-	0.393	2010
methane	PR equation	0.01	0.00332	2190
Berea sandstone	2030	-	5	800

2.2. Mathematical Model

Mathematical models of the multiphase flow and heat transfer include mass balance equations, heat balance equations, additional source terms of mass and energy, and initial and boundary conditions. The basic governing equations for the multiphase flow in the porous rock and the reaction kinetics of the NGH dissociation are presented in Table 3.

The effects of the geo-stress are also coupled with the transportation and dissociation process of the NGH in the porous media. Based on the assumptions of stress and strain linearity and the reversibility of medium deformation, Biot et al. [45] proposed the pore elastic constitutive equation of fluid saturated porous media. Detournay et al. [46] proposed the pore elastic constitutive equation illustrated in Equation (1), and defined volumetric strain as follows, under isotropic compressive stress:

$$\varepsilon_V = \frac{\sigma}{2G} - (\frac{1}{6G} - \frac{1}{9K_T})\delta\sigma + \frac{1}{3H'}\delta P_T \quad (1)$$

$$\varepsilon_V = 3\varepsilon = \frac{1}{K}(\sigma - \alpha P_T) \quad (2)$$

where ε_v is volumetric strain, G is the shear modulus, K_T is bulk modulus, δ is a unit matrix, H' is the constitutive constant (stress-strain coupling of fluid), σ is confining pressure, and P_T is pore pressure.

Usually, the effective stress is calculated, based on the test results of variable confining pressure experiments. There are various forms of effective stress. In 1923, Terzaghi proposed the calculation formula of effective stress:

$$\sigma' = \sigma - p \quad (3)$$

In this study, the influence of effective stress in sandstone core was studied, and the effective stress coefficient was set to 1 in this study.

$$\sigma' = \sigma - \alpha p \quad (4)$$

where α is the effective stress coefficient. Fatt et al. [47,48] suggested that α could be set between 0.75 and 1. Knaap et al. [49], Hubbert et al. [50] and Zimmerman et al. [51] believed that the effective stress coefficient was set to 1 through the experimental results. In this study, $\alpha = 1$.

When the stress and pore pressure are known, the volumetric strain can be obtained by using the linear isotropic theory of pore elasticity. For the case of nonlinear volumetric deformation in porous rock, it was found that the fitting equation of stress–strain data collected in the Berea experiment was as follows (meeting the initial conditions $\sigma' = 0$, $\varepsilon_v = 0$) [52]:

$$\varepsilon_V = A'\sigma' - B'e^{-\sigma'/C'} + B'C' \quad (5)$$

where A', B', C' are the fitting constants [53], ε_V is volumetric strain.

Table 3. Different models of porous media methane hydrate dissociation flow.

	Sun et al. (2005)	**Nazridoust and Ahmadi. (2007)**	**Ruan et al. (2012)**	**Chen et al. (2016)**	**This Study**	
Modle Flow model Relative permeability	1-D Darcy's law Corey's model (1954)	2-D Darcy's law Corey's model (1954)	2-D Darcy's law Corey's model (1954)	2-D Darcy's law Corey's model (1954)	2-D Darcy's law Adapted Corey's model (1954)	
Permeability model	$k_{rw} = k\left(\frac{\frac{s_w}{s_w+s_g}-s_{wr}}{1-s_{wr}-s_{gr}}\right)^{nw}$, $k_{rg} = \left(\frac{\frac{s_g}{s_w+s_g}-s_{gr}}{1-s_{wr}-s_{gr}}\right)^{ng}$ $n_w = 4, n_g = 2, s_{wr} = 0.2, s_{gr} = 0.3;$	$k_D = k_{D0}(1-s_h)^N$ $N = 15$	$k_D = k_{D0}(1-s_h)^N$ $N = 11$	$k_D = k_{D0}(1-s_h)^N$ $N = 15$	$k_{rw} = \left(\frac{s_w-s_{wr}}{1-s_{wr}}\right)^{n_w}, k_{rg} = \left(\frac{s_g}{1-s_{wr}}\right)^{n_g}$ $n_w = 0.6, n_g = 1.42;$	where K_{rw} and k_{rg} are the relative permeability of water and gas, S_{wr} is the irreducible saturation of water.
	$k_D = \begin{cases} 5.51721 \times (\varphi_e)^{0.86}, \varphi_e < 0.11 \\ 4.84653 \times 10^8 \times (\varphi_e)^{9.13}, \varphi_e \geq 0.11 \end{cases}$				$k_D = \begin{cases} 5.51721 \times \left(\frac{\varphi_0-\varepsilon_V}{1-\varepsilon_V}(1-s_h)\right)^{0.86}, \frac{\varphi_0-\varepsilon_V}{1-\varepsilon_V}(1-s_h) \geq 0.11 \\ k_{DO}(\frac{\varphi_0-\varepsilon_V}{1-\varepsilon_V}(1-s_h))^{1.2}, \frac{\varphi_0-\varepsilon_V}{1-\varepsilon_V}(1-s_h) \geq 0.11 \end{cases}$	where φ_O is absolute porosity, ε_v is volumetric strain, k_{DO} absolute permeability of the sandstone without contains hydrate, mD S_h is saturation of hydrate.
	Kim et al. (1987)	**Kim et al. (1987)**	**Kim et al. (1987)**	**Kim et al. (1987)**	**Kim et al. (1987)**	
Dissociation rate (k_d, A_d)	$\dot{m}_g = k_d A_S(f_e - f), k_d = 4.4 \times 10^{-16}$				$\dot{m}_g = k_d M_g A_d\left(p_{eh} - p_g\right) = k_d^o e^{-\frac{\Delta E}{RT}} M_g A_d\left(P_{eg} - P_g\right)$	where P_{eh} is the equilibrium pressure, P_g is the methane pressure, A_d is reacting surface of hydrate, K_d^0 is the intrinsic constant, R is the universal gas constant, ΔE is an activation energy.
Dissociation constant k_d (kmol/Pa.s.m^2)	$k_d^0 = 2.75 \times 10^{-12}$	$k_d^0 = 8.06$ $\Delta E = 77.33 \times 10^3$ J	$k_d^0 = 36$ $\Delta E = 81.08 \times 10^3$ J	$k_d^0 = 124$ $\Delta E = 78.15 \times 10^3$ J	$k_d^0 = 36$ $\Delta E = 81.08 \times 10^3$ J	$\varphi_e = \varphi_o(1-s_h)$ where φ_e is the effective porosity of porous media.
Surface area of hydrate per unit volume A_d	$A_d = \sqrt{\frac{\varphi_e^3}{2K_D}}$	$A_d = \varphi_0 S_h A_{geo}, 2r = 16\ \mu m$ $A_{geo} = 3.75 \times 10^5\ m^2/m^3$	$A_d = \sqrt{\frac{\varphi_e^3}{2K_D}}$	$A_d = \varphi_0 S_h A_{geo}, 2r = 16\ \mu m$ $A_{geo} = 3.75 \times 10^5\ m^2/m^3$	$A_d = \sqrt{\frac{\varphi_e^3}{2K_D}}$	where M_w and M_h are molecular weights of water and hydrate.
The heat transfer Enthalpy, internal energy (J/Kg)	$\Delta H_d = 446.12 \times 10^3 - 132.638T$	$\Delta H_d = 473.63 \times 10^3 - 140.117T$	Sun et al. (2005)	$\Delta H_d = 473.63 \times 10^3 - 140.117T$	$\dot{m}_w = M_W N_H \dot{m}_g / M_g, -\dot{m}_h = M_h \dot{m}_g / M_g$ $q = \lambda_b(T_o - T)$ $\Delta H_d = \begin{cases} 215.59 \times 10^3 - 394.945T, 248K < T < 273K \\ 446.12 \times 10^3 - 132.638T, 273K < T < 298K \end{cases}$	where q is boundary heat flux, T_O is air temperature, λ_b is the boundary heat transfer coefficient determined by the heat transfer coefficient of the rubber sleeve and the ambient convection intensity.

Table 3. *Cont.*

	Sun et al. (2005)	Nazridoust and Ahmadi. (2007)	Ruan et al. (2012)	Chen et al. (2016)	This Study
Continuity equation of different fluid phases are: Momentum equation	$\frac{\partial}{\partial t}(\varphi_0 \rho_k S_k) + \frac{\partial}{\partial x}(\rho_k S_k) = \dot{m}_k$ $(k = h, g, w)$	$-\nabla.\rho_k \overrightarrow{u_k} + \dot{m}_k = \frac{\partial}{\partial t}(\varphi_0 \rho_k S_k)$ $(k = h, g, w, i)$	$-\frac{1}{r}\frac{\partial}{\partial r}(r\rho_k v_{kr}) + \frac{\partial}{\partial x}(\rho_k v_{kx}) + \dot{q}_k$ $+\dot{m}_k = \frac{\partial}{\partial t}(\varphi_0 \rho_k S_k)(k = g, w)$ $\dot{m}_h = \frac{\partial}{\partial t}(\varphi_0 \rho_h S_h)$	Nazridoust and Ahmadi. (2007)	$-\nabla.\rho_k \overrightarrow{u_k} + \dot{m}_k = \frac{\partial}{\partial t}(\varphi_0 \rho_k S_k)$ $(k = h, g, w)$ where ρ is the density, m_k is the mass rate of dissociation formation substance, φ_0 is the porosity, S is the saturation, μ_k is the fluid velocity. The subscripts h, g, w corresponds to hydrate, gas and water in multiphase systems, respectively. $u_k = -\frac{k_D k_{rk}}{\mu_k}\nabla p_k, (k = g, w)p$ where u_k is the relative permeability of phase k, K_D is the absolute permeability of hydrated sandstone, K_{rk} is the relative permeability of phase k, and P is fluid pressure
Energy equation	$\frac{\partial}{\partial t}\begin{bmatrix}(1-\varphi_o)\rho_R H_R + \varphi_O S_h \rho_h H_h \\ +\varphi_O S_w \rho_w H_w + \varphi_O S_g \rho_g H_g\end{bmatrix}$ $+\frac{\partial}{\partial x}\left(\rho_w v_w H_w + \rho_g v_g H_g\right)$ $= \frac{\partial}{\partial x}\left(\lambda \frac{\partial T}{\partial x}\right) + q$	$\frac{\partial}{\partial t}\begin{bmatrix}(1-\varphi_o)\rho_R C_R T + \varphi_O S_h \rho_h C_h T \\ +\varphi_O S_w \rho_w C_w T + \varphi_O S_g \rho_g C_g T\end{bmatrix} C_K$ $+\nabla T.(\rho_w C_w \overrightarrow{u}_w + \rho_g C_g \overrightarrow{u}_g) - \nabla.(\lambda_e \nabla T) = \dot{Q}_h$ $\dot{Q}_h = \frac{-\dot{m}_H (c+dT)}{M_H}$ C = 56.599J/mol, d = −16.744J/mol K	$\frac{1}{r}\frac{\partial}{\partial r}\left(rk_c \frac{\partial T}{\partial r}\right) + \frac{\partial}{\partial x}\left(k_c \frac{\partial T}{\partial x}\right)$ $-\frac{1}{r}\frac{\partial}{\partial r}\left(r\rho_g v_{gr} h_g + r\rho_w v_{wr} h_w\right)$ $-\frac{\partial}{\partial x}\left(\rho_g v_{gr} h_g + \rho_w v_{wr} h_w\right)$ $+\frac{\partial}{\partial x}(\rho_k v_{kx}) + \dot{q}_g h_g + \dot{q}_w h_w + \dot{q}_h + \dot{q}_{in}$ $= \frac{\partial}{\partial t}\left[(1-\varphi)\rho_r h_r + \varphi\left(h_h \rho_h S_h + h_g \rho_g S_g + h_w \rho_w S_w\right)\right]$	Nazridoust and Ahmadi. (2007)	$-\nabla.\rho_k \overrightarrow{u_k} + \dot{m}_k = \frac{\partial}{\partial t}(\varphi_0 \rho_k S_k)$ $(k = h, g, w)$ where ρ is the density, m_k is the mass rate of dissociation formation substance, φ_0 is the porosity, S is the saturation, μ_k is the fluid velocity. The subscripts h, g, w corresponds to hydrate, gas and water in multiphase systems, respectively. $u_k = -\frac{k_D k_{rk}}{\mu_k}\nabla p_k, (k = g, w)p$ where u_k is the relative permeability of phase k, K_D is the absolute permeability of hydrated sandstone, K_{rk} is the relative permeability of phase k, and P is fluid pressure $\frac{\partial}{\partial t}\begin{bmatrix}(1-\varphi_o)\rho_R C_R T + \varphi_O S_h \rho_h C_h T \\ +\varphi_O S_w \rho_w C_w T + \varphi_O S_g \rho_g C_g T\end{bmatrix} C_K$ $+\nabla T.\left(\rho_w C_w \overrightarrow{u}_w + \rho_g C_g \overrightarrow{u}_g\right) - \nabla.(\lambda_e \nabla T) = \dot{Q}_h$ where C is the heat capacity, T is the temperature, $\overrightarrow{u}$ is the internal energy, Subscript R represents rock, h is the enthalpy. λ_e is the effective thermal conductivity, $\dot{Q}_h$ is the source term of endothermic reaction based on hydrate dissociation. $\dot{Q}_h = -\dot{m}_h \Delta H_d - \phi\rho_g S_g \sigma_g \frac{\partial p_g}{\partial t} - \rho_g u_g \nabla p_g$ where $\dot{m}_h$ is the mass dissociation rate for methane hydrate, ΔH_d is the latent heat of hydrate during the dissociation of methane hydrate, σ_g is the Joule-Thomson throttling coefficient, $\sigma_g = -1.5 \times 10^{-4}$ $\lambda_e = (1-\varphi_0)\lambda_R + \varphi_0\left(s_h \lambda_h + s_w \lambda_w + s_g \lambda_g\right)$ where $\lambda_R, \lambda_h, \lambda_w, \lambda_g$ are thermal conductivity of rock, hydrate, water, gas, respectively.

Haghi et al. [54] derived the calculation equation of stress-dependent porosity of intact rock without considering the differences between particle compressibility and pore compressibility:

$$\varphi_t = \frac{\varphi_0 - \varepsilon_V}{1 - \varepsilon_V} \tag{6}$$

Then the effective porosity under the condition of different geo-stresses is:

$$\varphi_e = \frac{\varphi_0 - \varepsilon_V}{1 - \varepsilon_V}(1 - s_h) \tag{7}$$

A new permeability formula under effective stress can be obtained as follows:

$$k_D = \begin{cases} 5.51721 \times \left(\frac{\varphi_0 - \varepsilon_V}{1 - \varepsilon_V}(1 - s_h)\right)^{0.86}, \frac{\varphi_0 - \varepsilon_V}{1 - \varepsilon_V}(1 - s_h) < 0.11 \\ k_{DO}\left(\frac{\varphi_0 - \varepsilon_V}{1 - \varepsilon_V}(1 - s_h)\right)^{1.2}, \frac{\varphi_0 - \varepsilon_V}{1 - \varepsilon_V}(1 - s_h) \geq 0.11 \end{cases} \tag{8}$$

3. Results and Discussions

3.1. Model Validation

The gas production vs. time in the simulation and Masuda's experiment are presented in Figure 2. The simulation results showed the generation of methane gas in this study was slightly delayed, compared to experimental results. The temperature of the inspecting points (P1, P2, P3) vs. time in the simulation and Masuda's experiment are presented in Figure 3. It can be seen that when the time t was in the range of 0–100 min, closer to the outlet, the faster the temperature dropped, which was generally consistent with Masuda's experimental results. The minimum temperature of the three monitoring points in the simulation was lower than that of the Masuda experiment. The R-square values of the three temperature monitoring points were 0.882, 0.799, and 0.852, respectively. The pore pressure at the far-field boundary vs. time is presented in Figure 4. The overall trend of the pressure drop at the far end in the simulation experiment was consistent with the results of the Masuda experiment. The R-square of the far end boundary pressure was 0.890. The variations between the simulation and experimental results were caused by the heterogeneous distribution of the different phases, as well as the heterogeneous pore structure in the Berea sandstone. Considering the influence of pore structure, hydrate heterogeneity, and the application of the mathematical model on the experiment, the simulation results were believed to be in good agreement with the Masuda experiment.

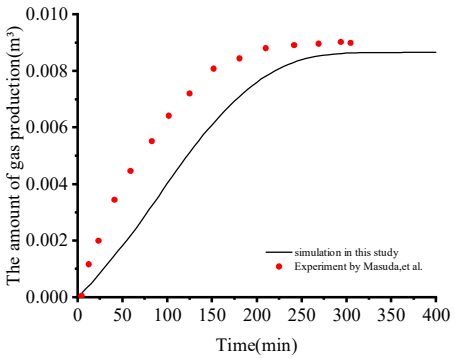

Figure 2. Gas production vs. time in the simulation experiment and Masuda's experiment [43].

As shown in Appendix A, the gas production of methane vs. time varies in literatures and in this study. The reasons lie in the fact that the initial hydrate saturation in some literature [19–25,43] was 0.443, while it was 0.501 in some others [17,18,26,28,41] and in this study. Zhang et al. [18] and Ruan's [20] gas production curves were in good agreement with the trials; however, Zhang only simulated gas production. The far-field boundary pressure was not simulated by Ruan et al. Chen et al. [23] simulated the pressure and temperature at the monitoring point without the gas generation. Additionally, the findings in this

study and the literature [17,21–25,27] demonstrated that the early-stage gas generation rate was lower. The gas production rate was relatively higher, according to modeling results from Song et al. [44]. Overall, the simulation results in this study agreed well with the experimental benchmark data in far-field boundary pressure, temperature, and gas production, by assuming a homogenous initial distribution of the hydrate, water and methane in Berea sandstone.

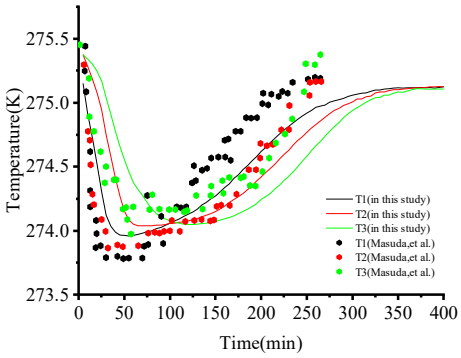

Figure 3. Temperature (T1, T2, T3) vs. time in the simulation experiment and Masuda's experiment [43].

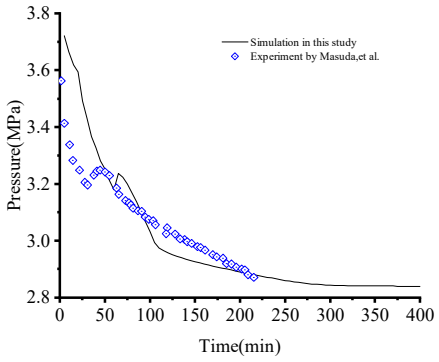

Figure 4. Pore pressure vs. time in the simulation experiment and Masuda's experiment [43].

As shown in Appendix B, Nazridoust et al. [21] the distal pressure did not significantly change at the start of the simulation, and the distal pressure of Chen et al. [23] was at its lowest point after 125 min of reaction time. Furthermore, Wan et al. [41] found that although the downward pressure trend throughout the earlier time was consistent, the downward pressure trend between 50 and 200 min was rather sluggish, and none of their results included small peaks. Small peaks were visible in the simulation findings from this work. The small peak predicted by Song et al. [44] and the trials were essentially in agreement; however, the pressure value remained high after the small peak arrived. The trials 'small peak fluctuated as the pressure lowered to roughly 3.2 MPa, and the small peak anticipated in this work exhibited the same behavior, but it occurred about 20 min later. Overall, the simulation results in this study agreed well with the experimental benchmark data in far-field boundary pressure.

Theoretically, the closer to the outlet, the lower the temperature and the earlier the dissociation of the hydrate. However, as shown in Appendix C, Chen et al.'s findings [23] did not support this conclusion. In terms of the temperatures at each monitoring point in the sandstone core during hydrate dissociation, the findings in this study and the literature [17–22,24–26,41] basically predicted the correct result. That is, the temperature at T1 decreased earlier than that at T2, and the temperature at T2 decreased earlier than that at T3. In this study and in [17,21,26,27,41], the monitoring point temperature was even lower, while in [19,20,23,24] it was higher. Since their boundary heat transfer coefficients were (50, 41.8, 16.6, 45.4, 45, 50) W/(m^{2}K), this study holds that the result was mostly caused by the boundary's uneven heat transmission. Considering the gas production at the outlet, the

far-field boundary pressure and the temperature at the monitoring point, the curve fits of this study were good, compared with most previous research.

3.2. Effect of Initial Gas Saturation

The effects of initial gas saturation (0.1, 0.2, 0.25, 0.3, 0.4) on hydrate dissociation were investigated in this section. Other simulation conditions, except the initial gas saturation, were maintained. As shown in Figure 5, natural gas production with different initial gas saturations fluctuated over time. When the outlet valve was opened, gas production first increased sharply and then dropped steadily to zero over time. The fundamental cause for the first peak was that the gas tended to flow out when the outlet valve opened, due to the pressure difference between the inside and outside of the core. When the hydrate gradually decomposed, the difference between gas fugacity and equilibrium fugacity grew, promoting hydrate decomposition and increasing the gas production rate to the second peak. The value, $t_{90\%}$ (referring to the required time of 90% NGH dissociating in the core), decreased with increase of the initial gas saturation, as shown in Figure 6, which also showed that the higher the initial gas saturation, the faster the NGH decomposed.

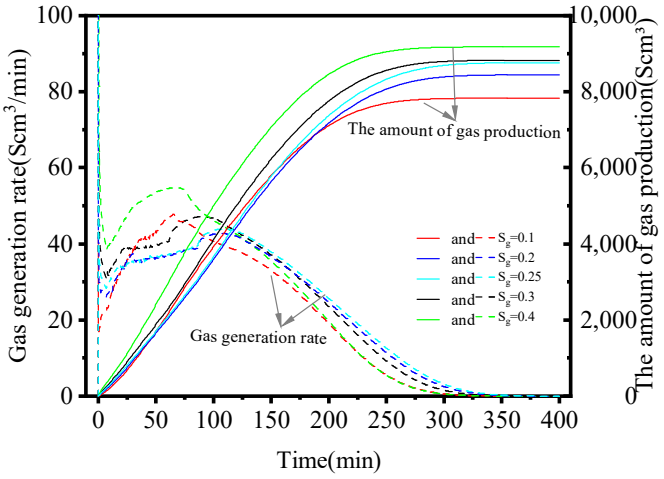

Figure 5. Gas production rate and cumulative gas production vs. time under different initial gas saturations.

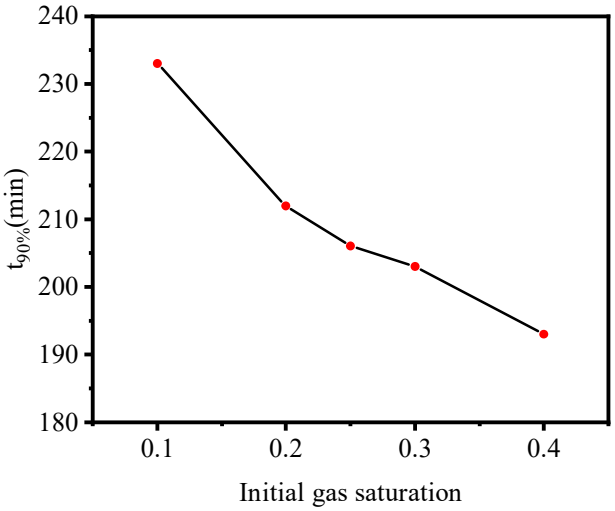

Figure 6. The value $t_{90\%}$ vs. initial gas saturation.

3.3. Effect of Outlet Pressure

The effects of outlet pressure (2.52 MPa, 2.68 MPa, 2.84 MPa, 3.00 MPa, 3.16 MPa) on hydrate dissociation were investigated in this section. Other simulation conditions,

except the outlet pressure, were maintained. As shown in Figure 7, gas production and cumulative production fluctuated over time as the outlet pressure changed. The study found that natural gas production had four stages and two peaks, which were basically the same characteristics as mentioned earlier. The NGH in the core did not entirely dissociate in the first 400 min when the outlet pressure exceeded 3.16 MPa. Additionally, it was evident that when outlet pressure fell, a greater overall amount of gas was generated. The residual gas in the core varied under various pressure differences, which led to different cumulative gas production. The value,$t_{90\%}$, decreased with a decrease in the outlet pressure, as shown in Figure 8, which also showed that the lower the outlet pressure, the faster the natural gas hydrate decomposed.

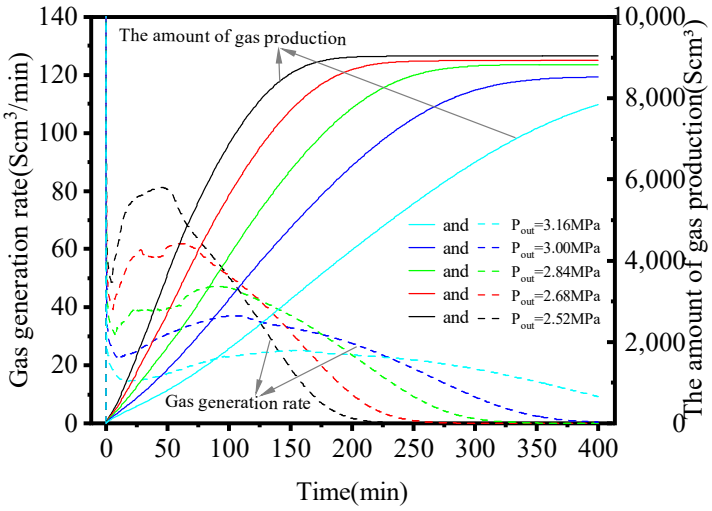

Figure 7. Gas production rate and cumulative gas production vs. time under different outlet pressure.

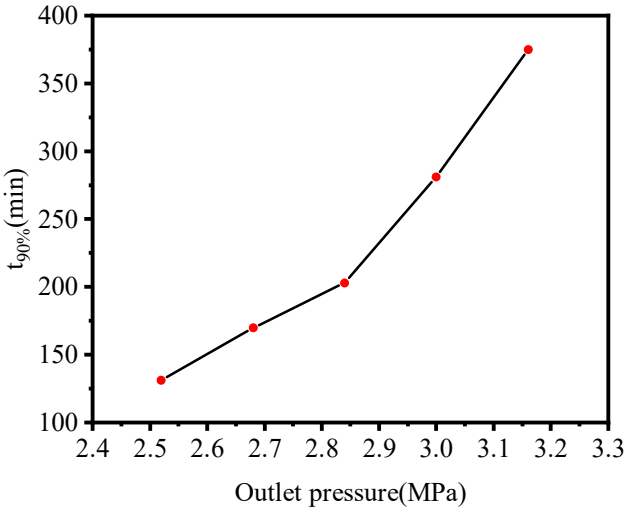

Figure 8. The value $t_{90\%}$ vs. outlet pressure.

3.4. Effect of Initial Temperature

The effects of initial temperatures (273.45 K, 274.45 K, 275.45 K, 276.45 K, 277.45 K) on hydrate dissociation were investigated in this section. Other simulation conditions, except the initial temperatures, were maintained. As shown in Figure 9, at higher initial temperatures, natural gas production and cumulative natural gas production fluctuated over time as the initial temperature changed, and as the initial temperature increased, the rate of natural gas hydrate dissociation accelerated. The total production of gas did not change much, though. The value, $t_{90\%}$, decreased with increasing initial temperatures, as shown in Figure 10, which also showed that the higher the initial temperatures, the

faster the natural gas hydrate decomposed. As shown in Figure 11, it was discovered that, under adiabatic conditions, the gas generation rate rose instantly in the beginning and then gradually fell until it reached zero. As the final cumulative gas production was 2800 Scm^3, no new gas was generated, so it could be concluded that the hydrate would not decompose under adiabatic conditions (insufficient energy).

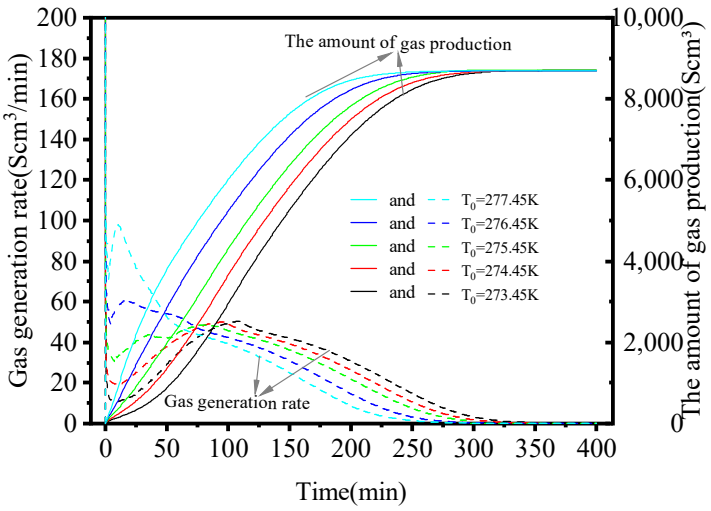

Figure 9. Gas production rate and cumulative gas production vs. time at different initial temperature.

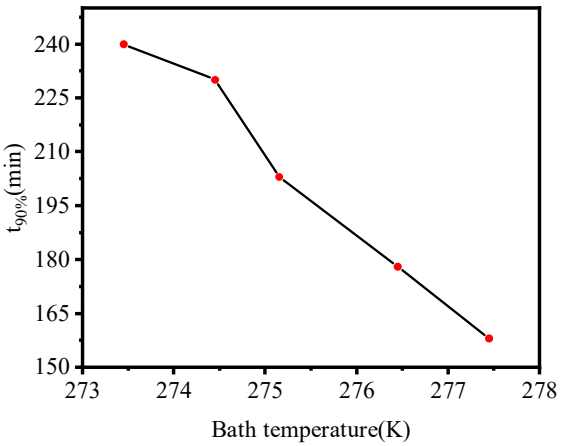

Figure 10. The value $t_{90\%}$ vs. initial temperature.

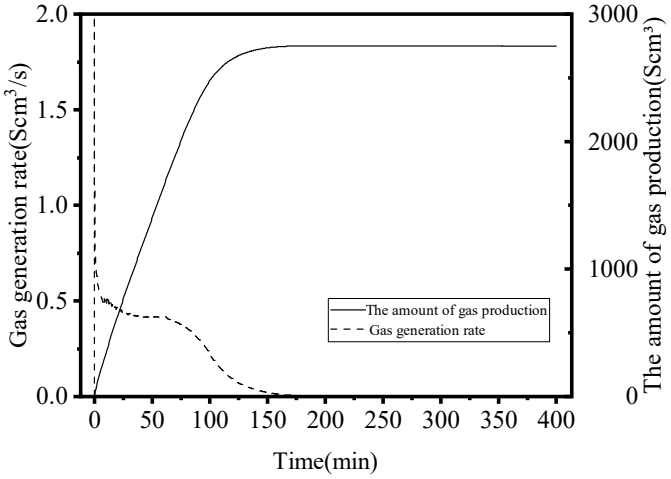

Figure 11. Gas production rate and cumulative gas production vs. time under adiabatic boundary conditions.

3.5. Effect of Absolute Permeability

The effects of absolute permeability (10 mD, 50 mD, 98.97 mD, 150 mD, 200 mD) on hydrate dissociation were investigated in this section. Other simulation conditions, except the absolute permeability, were maintained. As shown in Figure 12, variation of absolute permeability caused gas production rate and cumulative gas production to fluctuate with time. The gas production rate and cumulative gas production for 10 mD absolute permeability were different from the other four data, and the gas production rate was very low. This was because reduced absolute permeability limited fluid flowability and decreased the pressure driving force of hydrate dissociation, resulting in a lengthier hydrate dissociation process. The value, $t_{90\%}$, decreased with an increase in the absolute permeability, as shown in Figure 13, which also showed that the higher the absolute permeability, the faster the natural gas hydrate decomposed.

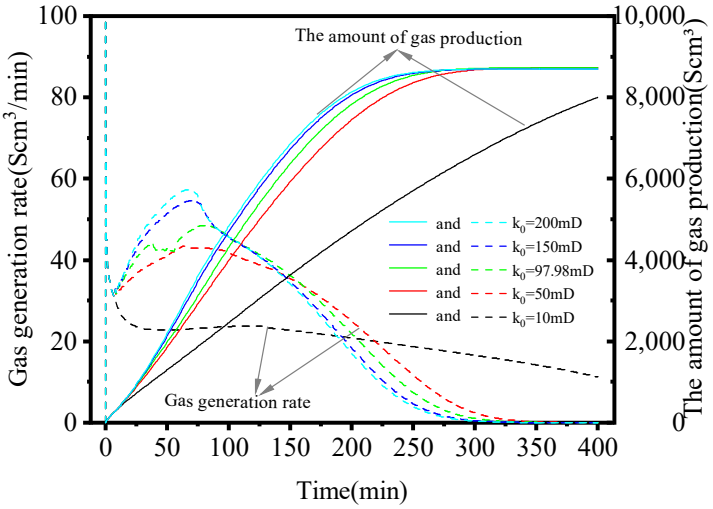

Figure 12. Gas production rate and cumulative gas production vs. time under different absolute.

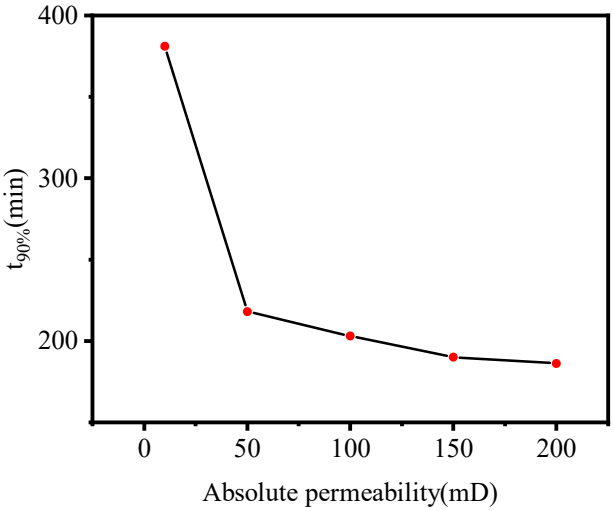

Figure 13. The value $t_{90\%}$ vs. absolute permeability.

3.6. Effect of Geo-Stress

As early as the 1940s, some researchers in other countries began to investigate the fluctuation of porosity and permeability with confining pressure. Fatt et al. [47,48], Gray et al. [53], and Mclatchie et al. [55] investigated the effect of reservoir stress fluctuations on rock permeability and porosity, and the researchers confirmed that porosity and permeability steadily declined as effective stress increased. In the late 1980s, China conducted a substantial study on reservoir stress sensitivity. Research [47,48,51–56] showed that the porosity and permeability

of the reservoir decreased when effective stress increased. Furthermore, the stress sensitivity effect was particularly noticeable in low permeability reservoirs.

Zhu and Wang et al. [56] reported the stress-related porosity data of five different sandstones under isotropic effective stress conditions. As shown in Figure 14, the effective stress range of 0–30 MPa appeared in the data and the fitting curves of volumetric strain and stress-related porosity of Equations (5) and (6) to assess the validity of the aforesaid fitting correlation equation for Berea sandstone. The certain value of the fitting constants are displyed in Table 4.

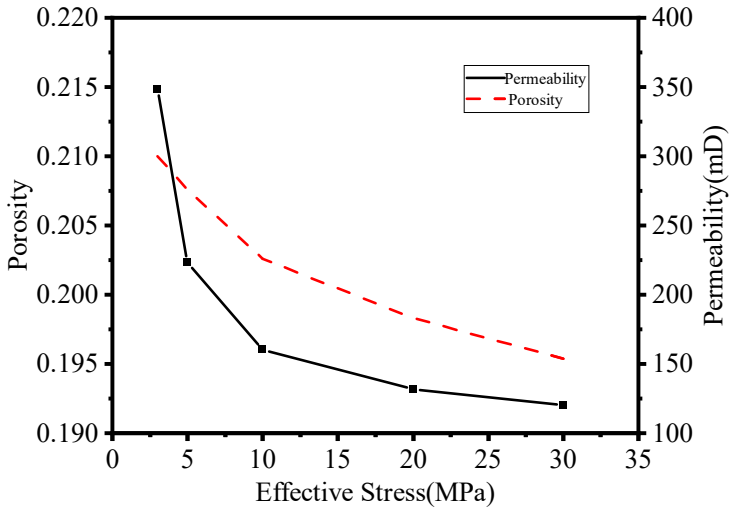

Figure 14. Fitted curves of porosity and permeability of Berea sandstone vs. effective stress in Zhu and Wang's experimental data [56].

Table 4. Fitting constants in Zhu and Wang experiments.

Rock	A'	B'	C'
Berea sandstone	0.183	0.01859	9.842

Based on Masuda's hydrate core decomposition experiment, the effective stress (5 MPa, 15 MPa, and 25 MPa) was changed by varying the confining pressure of the sandstone core, and numerical models were built for the evolution of physical properties of hydrate sandstone cores under different stresses.

Figure 15a,b show the volume of gas hydrate in the cores considering, or not considering, the effect of ground stress. The average volume fraction in the core, considering the geo-stress, was higher than that without considering the geo-stress at the same time point, which indicated that the effect of geo-stress reduced the decomposition rate of natural gas hydrate in sandstone core. The volume fraction of methane in the core without considering, or considering, the effect of geo-stress is shown in Figure 16a,b. The average volume fraction in the core, considering the geo-stress, was lower than that without considering the geo-stress at the same time, which indicated that the effect of geo-stress reduced the gas production rate in sandstone core. Figure 17 also illustrates this point. The temperature in the core without considering, or considering, the effect of geo-stress is shown in Figure 18a,b. In the process of the temperature dropping, caused by endothermic reaction, the average core temperature considering geo-stress effect was higher than that without considering geo-stress. In the process of the temperature rising, caused by heat transfer, the average core temperature considering geo-stress was lower than that without considering geo-stress, which indicated that the effect of geo-stress slowed down the efficiency of the heat and mass transfer in the sandstone core, leading to slower dissociation and transportation rates of the NGH.

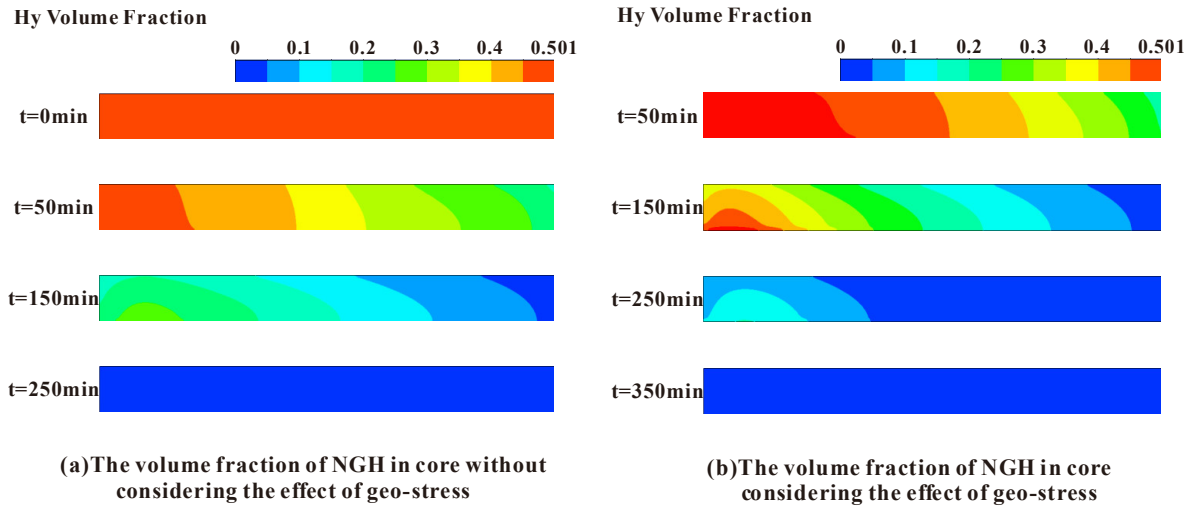

Figure 15. Hydrate volume fraction in the core at different times.

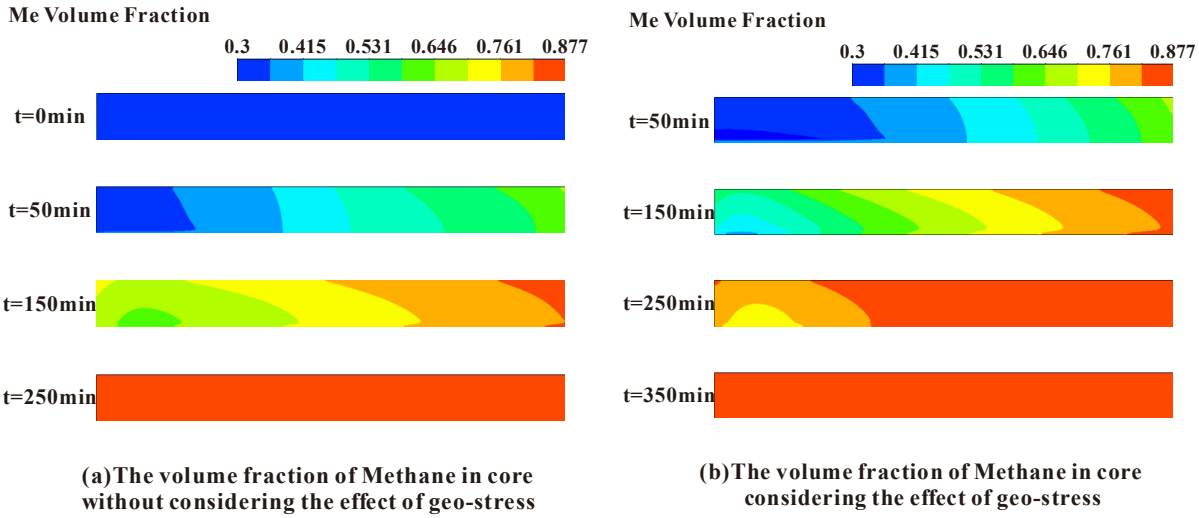

Figure 16. Methane volume fraction in the core at different times.

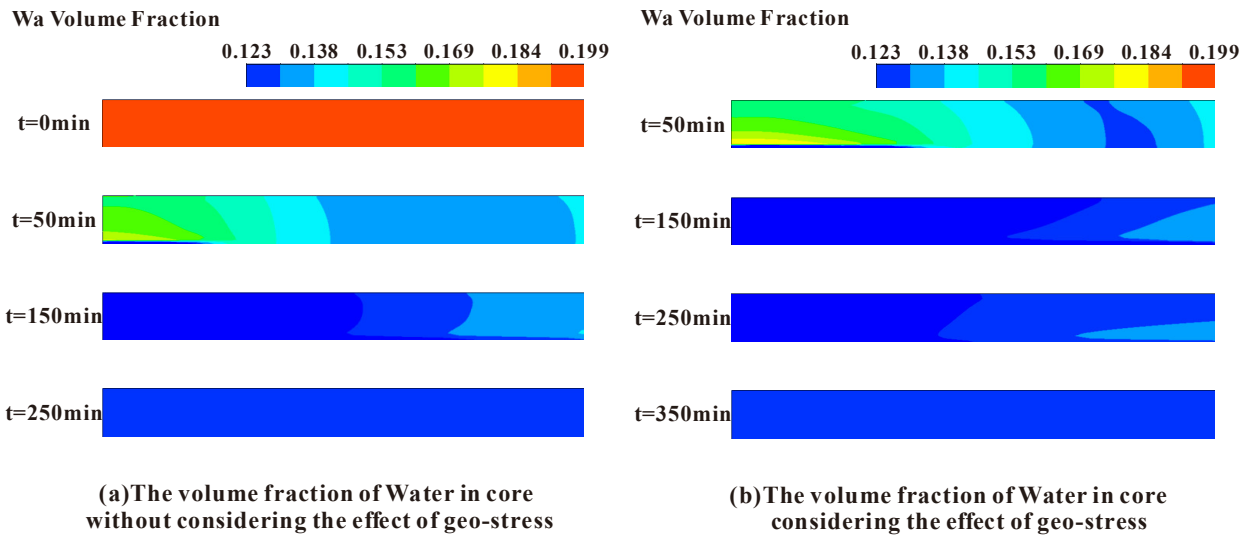

Figure 17. Water volume fraction in the core at different times.

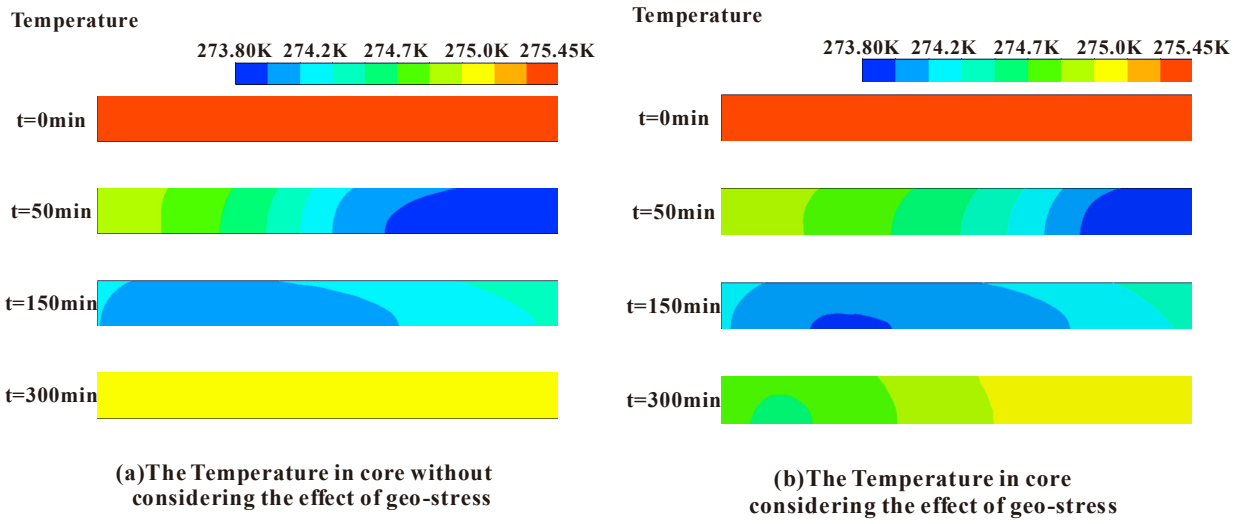

Figure 18. Temperature distribution in the core at different times.

As shown in Figure 19, natural gas production and cumulative natural gas production fluctuated with time under different effective stresses. The gas production rate graph shows that, at 125 min, before the reaction, the instantaneous gas production rate, without taking the effect of effective stress into account, was higher than that under the effect of effective stress. The rate of gas production decreased as effective stress increased. In addition, as the effective stress increased, the time to drop to zero for the corresponding gas production rate increased, which also meant that the time for the hydrate dissociation increased. This was because the effective stress decreased the amount of pore space, which lowered the core's permeability and porosity. The permeability and porosity in the core decreased as the effective stress increased. The slower the heat convection, the lower the mass transfer efficiency, and the longer it took for the hydrate to dissociate, the smaller the permeability, so, consequently, the longer the completion date for gas production from the use of natural gas hydrates. The cumulative gas output showed that, under various effective stress levels, the final cumulative gas output was equal. The time it took to reach the final cumulative gas output increased with the effective stress. This indicated that the effective stress decreased the permeability of the core, hence decreasing the rate of hydrate decomposition and mining efficiency. However, it had no impact on the hydrate decomposition's overall cumulative gas generation. As shown in Figure 20, $t_{90\%}$ rose as effective stress increased. This was because the increase of effective stress led to the volume shrinkage of pore space, thus reducing the permeability and porosity of sediments. Low permeability slowed thermal convection, which slowed down the pressure drop from one end of the core to the outlet and reduced mass transfer efficiency. This slowed down hydrate decomposition, which increased the time it took to produce gas from natural gas hydrates and reduced their exploitation efficiency. Therefore, the natural gas hydrate production would be less effective as effective stress rose, under various effective stresses.

Under various effective stress levels, pore pressure at the far-field boundary varied over time as shown in Figure 21. The diagram shows that when the effective stress was low, the duration and size of the small peak were close and the pore pressure test curve was more like the experimental results of Masuda. The pore pressure test curve was significantly different from the experimental data of Masuda. With a rise in effective stress, the small peak value also gradually declined, and the small peak value's appearance time arrived later and later. Additionally, there was a small peak in several conditions, and this small peak in the pore pressure curve at the far-field boundary was not a coincidence; rather, it was one of the characteristics of the two-phase flow in porous media that was brought on by hydrate dissociation. In the case of hydrate dissociation, for instance, the inability of the gas to spread quickly led to an increase in local pore pressure. This demonstrated that the impact of effective stress caused a reduction in pore space volume, which caused a

reduction in the core's porosity and permeability. As a result, the gas produced by hydrate decomposition could not be discharged quickly and accumulated in the core, increasing core pressure and further impeding hydrate decomposition. Additionally, hydrate breakdown was slowed down by increasing effective stress.

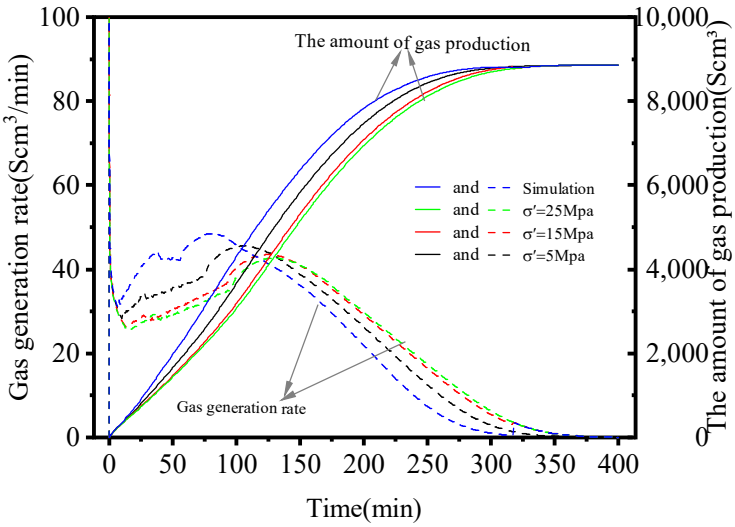

Figure 19. Gas production rate and cumulative gas production vs. time under different effective stresses.

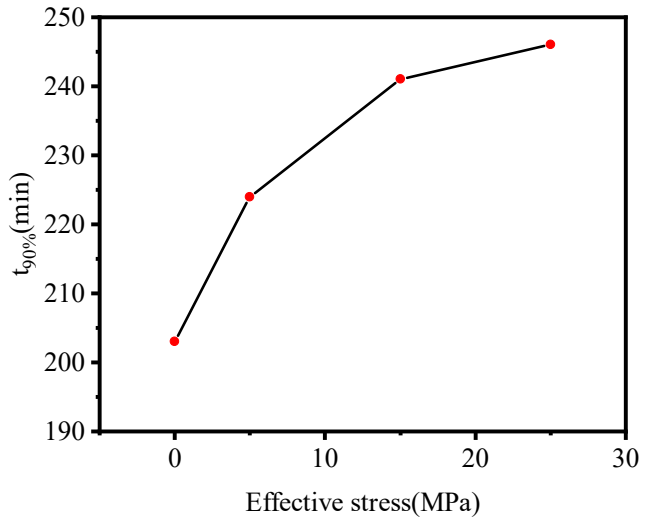

Figure 20. The value $t_{90\%}$ vs. confining pressure.

Three monitoring points' temperatures over time, and under various effective stress levels, are shown in Figure 22. The minimum temperature considering effective stress was higher than it was without considering effective stress 125 min before decompression, as shown in Figure 22. The increasing rate of temperature recovery (the heat transfer-induced temperature recovery process) was lower than it would be without taking effective stress into account. This was due to the decrease in effective stress, which lowered the core's porosity and permeability, and, moreover, slowing down the pace of hydrate dissociation to achieve a late minimum temperature. Additionally, it can be seen from a comparison of Figure 22a–c that the greater the effective stress, the later the minimum temperature appeared. This was because the core's porosity and permeability decreased as the effective stress increased. The low permeability restricted the efficiency of the heat and mass transfer by the fluid flow, leading to a slow dissociation and transportation rate of the NGH.

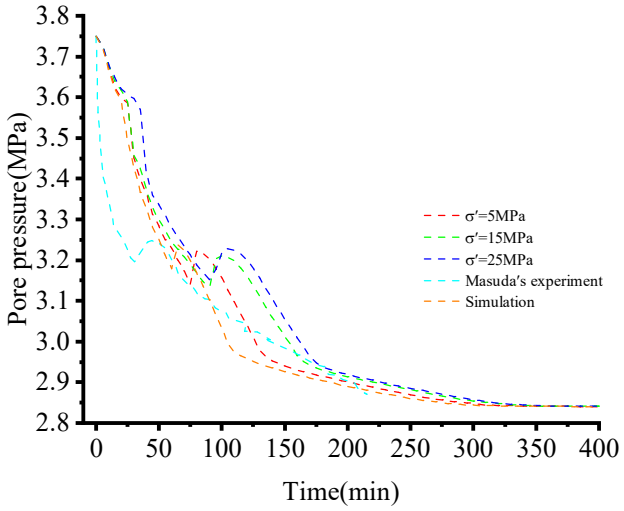

Figure 21. Far field pressure vs. time of the core for different effective stresses.

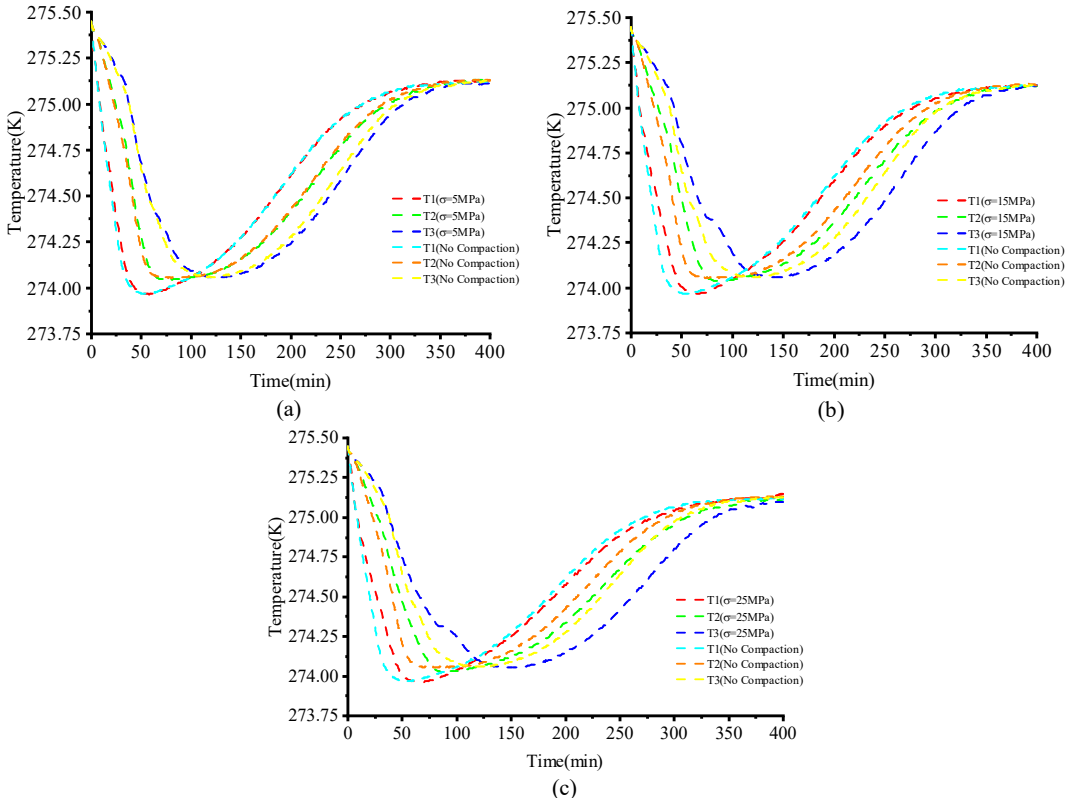

Figure 22. Temperature of monitoring points vs. time under different effective stress conditions and without considering stress. Subgraph (**a**–**c**) show that the temperature of monitoring points vs. time under the effective stress of 5 MPa, 15 MPa, 25 MPa and without considering stress.

4. Conclusions

In this study, an axisymmetric two-dimensional model was developed to simulate the depressurization decomposition process of natural gas hydrate in Berea sandstones. A mathematical model that considered fluid heat, mass transport, multiphase flow mechanics, and the kinetics of hydrate decomposition, was established. FLUENT was employed to solve the basic governing equations of multi-phase flow and UDF was used to program the hydrate dissociation model and modified permeability model during NGH dissociation and transport. The simulation results were then validated by Masuda's experimental data, and multi-parametric analysis was performed. The following conclusions could be achieved:

- The established mathematical model and the simulation scheme were validated by historical matching with the experimental benchmark data.
- The sensitivity analysis of the parameters revealed that a higher absolute permeability, higher initial gas saturation, lower outlet pressure, and higher initial temperature advanced the decomposition rate of hydrate. Thus, an optimized production plan is essential to promote the extraction efficiency of the NGH.
- Geo-stress caused a decrease of the porosity and permeability in the porous rock, which restricted the efficiency of the heat and mass transfer by the fluid flow, leading to a slow dissociation and transportation rate of the NGH. Thus, it is essential to take geo-stress into consideration and balance the extracting efficiency and the well pressure, especially when the NGH is developed by depressurization.

In this paper, the numerical modeling on the core scale dissociation and transportation of NGH was conducted. Future study will focus on the development of NGH in its formation.

Author Contributions: Conceptualization, R.S.; Methodology, J.L.; Investigation, R.S.; Data curation, Y.D.; Writing—original draft, Y.D.; Writing—review & editing, J.L. and Y.S.; Funding acquisition, R.S. All authors have read and agreed to the published version of the manuscript.

Funding: This research was funded by the National Natural Science Foundation of China (Grant Number 51909225), and the Knowledge Innovation Program of Wuhan-Basic Research (Grant Number 2022010801010158).

Data Availability Statement: All the data and materials used in this paper are available from the corresponding author upon request.

Conflicts of Interest: The authors declare that they have no known competing financial interests or personal relationships that could have appeared to influence the work reported in this paper.

Appendix A

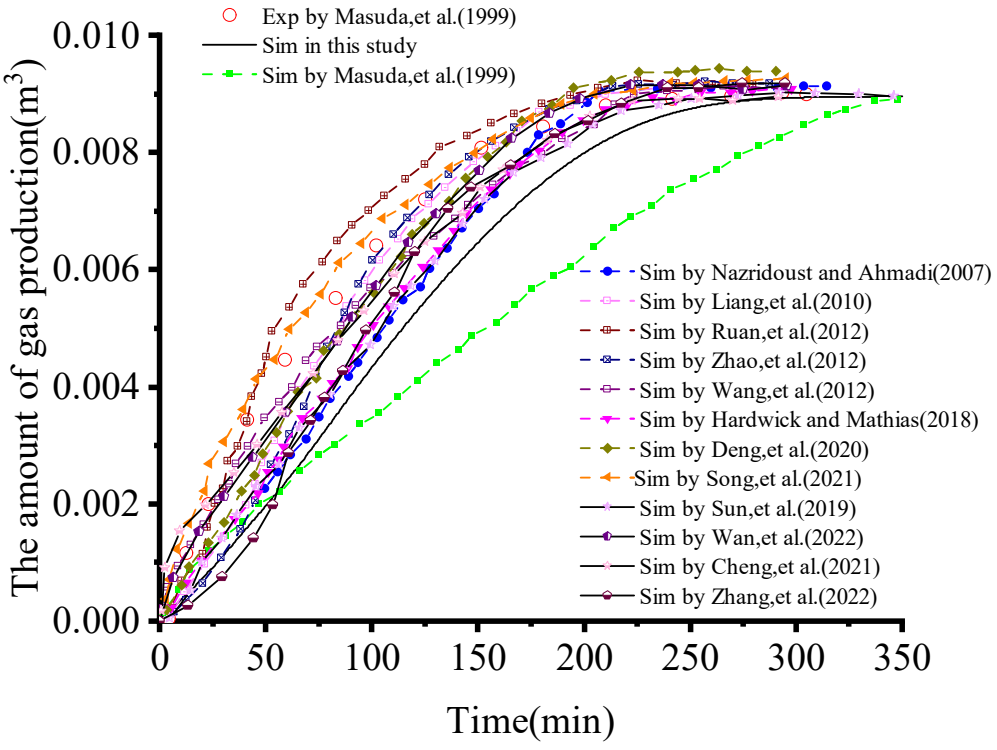

Figure A1. Gas production vs. time in this study and previous studies [17–28,41,43,44].

Appendix B

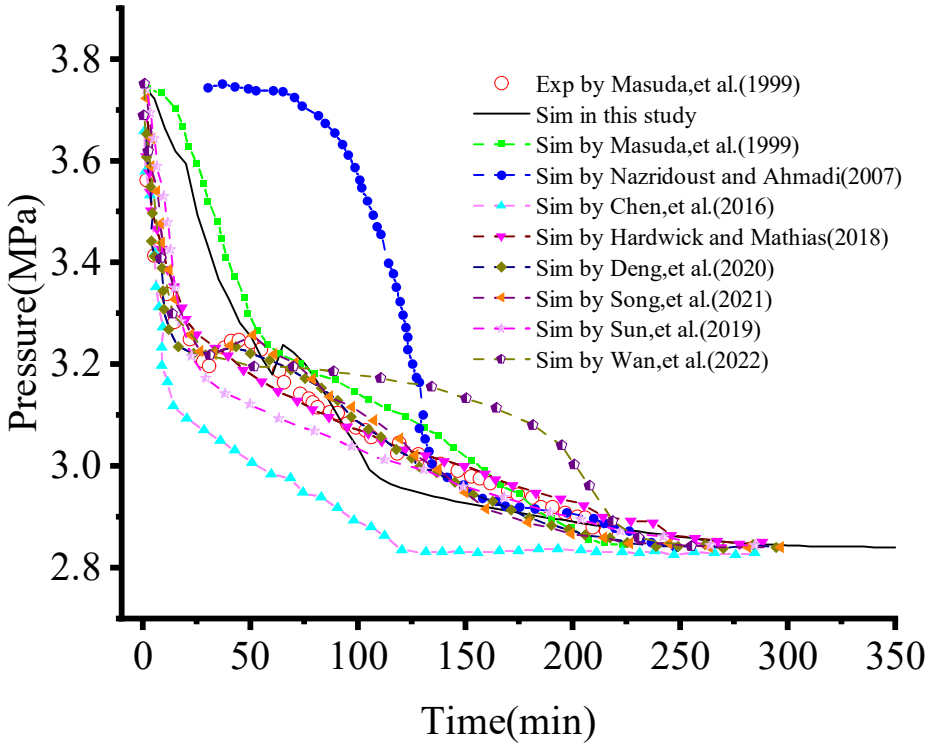

Figure A2. Far field pressure vs. time of this study and previous studies [17,20–22,27,41,43,44].

Appendix C

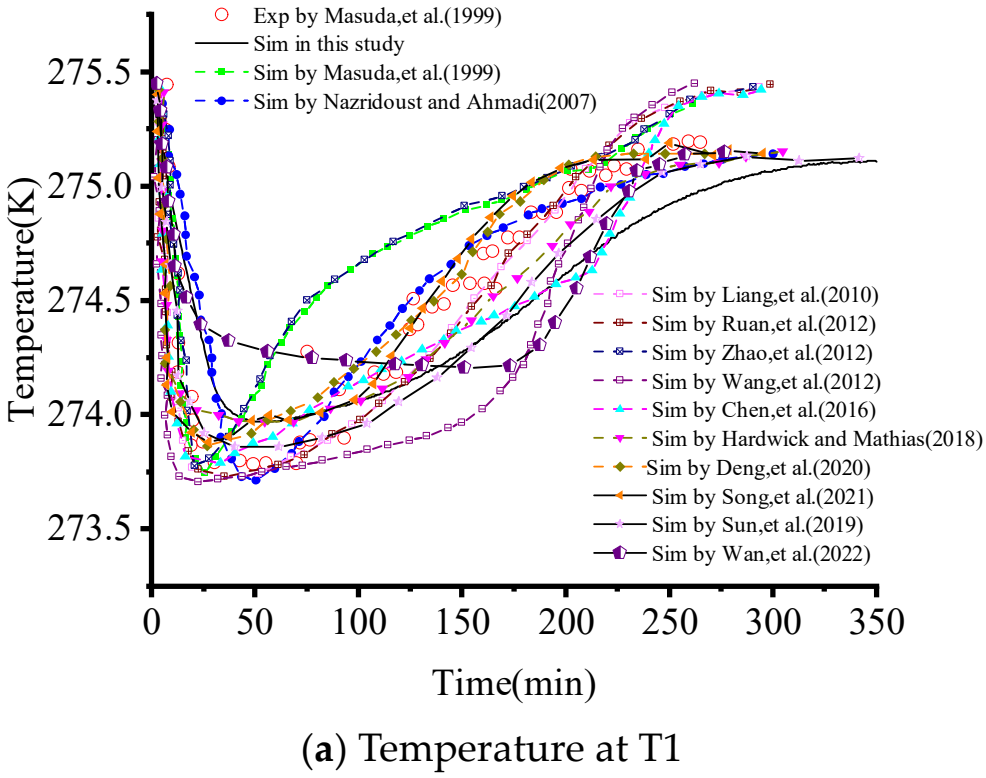

Figure A3. *Cont.*

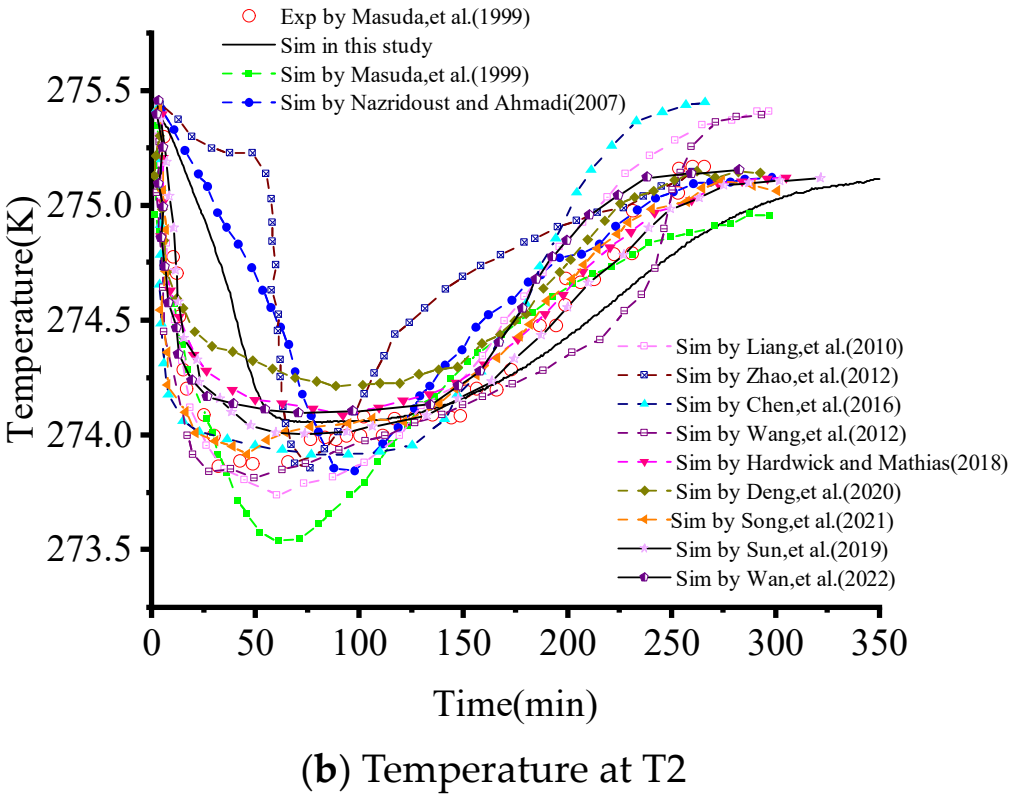

(**b**) Temperature at T2

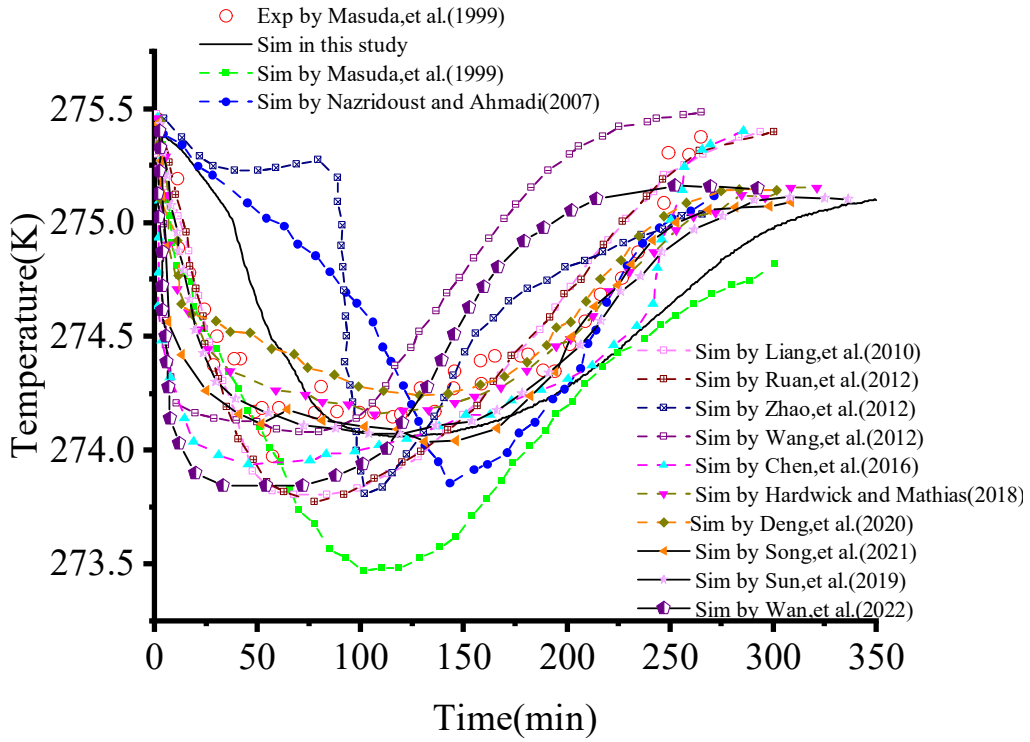

(**c**) Temperature at T3

Figure A3. Temperature at monitoring points vs. time of this study and previous studies [17,21–27,41,43].

References

1. Song, R.; Wang, Y.; Tang, Y.; Liu, J.; Yang, C. 3D Printing of natural sandstone at pore scale and comparative analysis on micro-structure and single/two-phase flow properties. *Energy* **2022**, *261*, 125226. [CrossRef]
2. Song, R.; Liu, J.; Yang, C.; Sun, S. Study on the multiphase heat and mass transfer mechanism in the dissociation of methane hydrate in reconstructed real-shape porous sediments. *Energy* **2022**, *254*, 124421. [CrossRef]
3. Song, R.; Sun, S.; Liu, J.; Yang, C. Pore scale modeling on dissociation and transportation of methane hydrate in porous sediments. *Energy* **2021**, *237*, 121630. [CrossRef]
4. Song, R.; Sun, S.; Liu, J.; Feng, X. Numerical modeling on hydrate formation and evaluating the influencing factors of its heterogeneity in core-scale sandy sediment. *J. Nat. Gas Sci. Eng.* **2021**, *90*, 103945. [CrossRef]
5. Yin, Z.; Linga, P. Methane hydrates: A future clean energy resource. *Chin. J. Chem. Eng.* **2019**, *27*, 2026–2036. [CrossRef]
6. Song, R.; Wang, Y.; Ishutov, S.; Zambrano-Narvaez, G.; Hodder, K.J.; Chalaturnyk, R.J.; Sun, S.; Liu, J.; Gamage, R.P. A comprehensive experimental study on mechanical behavior, microstructure and transport properties of 3D-printed rock analogs. *Rock Mech. Rock Eng.* **2020**, *53*, 5745–5765. [CrossRef]
7. Li, B.; Li, X.S.; Li, G.; Chen, Z.Y. Evaluation of gas production from Qilian Mountain permafrost hydrate deposits in two-spot horizontal well system. *Cold Reg. Sci. Technol.* **2015**, *109*, 87–98. [CrossRef]
8. Li, G.; Moridis, G.J.; Zhang, K.; Li, X.S. Evaluation of the gas production potential of marine hydrate deposits in the Shenhu Area of the South China Sea. In *Offshore Technology Conference*; OnePetro: Houston, TX, USA, 2010.
9. Feng, J.C.; Wang, Y.; Li, X.S.; Li, G.; Chen, Z.Y. Production behaviors and heat transfer characteristics of methane hydrate dissociation by depressurization in conjunction with warm water stimulation with dual horizontal wells. *Energy* **2015**, *79*, 315–324. [CrossRef]
10. Chong, Z.R.; Pujar, G.A.; Yang, M.; Linga, P. Methane hydrate formation in excess water simulating marine locations and the impact of thermal stimulation on energy recovery. *Appl. Energy* **2016**, *177*, 409–421. [CrossRef]
11. Chong, Z.R.; Yang, S.H.B.; Babu, P.; Linga, P.; Li, X.S. Review of natural gas hydrates as an energy resource: Prospects and challenges. *Appl. Energy* **2016**, *162*, 1633–1652. [CrossRef]
12. Wang, Y.; Lang, X.; Fan, S.; Wang, S.; Yu, C.; Li, G. Review on enhanced technology of natural gas hydrate recovery by carbon dioxide replacement. *Energy Fuels* **2021**, *35*, 3659–3674. [CrossRef]
13. Cai, J.; Xia, Y.; Lu, C.; Bian, H.; Zou, S. Creeping microstructure and fractal permeability model of natural gas hydrate reservoir. *Mar. Pet. Geol.* **2020**, *115*, 104282. [CrossRef]
14. Wang, X.; Dong, B.; Li, W.; Yu, M.; Song, Y. Microscale effects on methane hydrate dissociation at low temperature in the micro porous media channels by depressurization. *Int. J. Heat Mass Transf.* **2018**, *122*, 1182–1197. [CrossRef]
15. Makogon, Y.F. Natural gas hydrates–A promising source of energy. *J. Nat. Gas Sci. Eng.* **2010**, *2*, 49–59. [CrossRef]
16. Zhao, J.; Liu, D.; Yang, M.; Song, Y. Analysis of heat transfer effects on gas production from methane hydrate by depressurization. *Int. J. Heat Mass Transf.* **2014**, *77*, 529–541. [CrossRef]
17. Deng, X.; Feng, J.; Pan, S.; Wang, Z.; Zhang, J.; Chen, W. An improved model for the migration of fluids caused by hydrate dissociation in porous media. *J. Pet. Sci. Eng.* **2020**, *188*, 106876. [CrossRef]
18. Zhang, P.; Liu, B.; Hu, L.; Meegoda, J.N. Coupled multiphase flow and pore compression computational model for extraction of offshore gas hydrates. *Comput. Geotech.* **2022**, *145*, 104671. [CrossRef]
19. Liang, H.; Song, Y.; Chen, Y. Numerical simulation for laboratory-scale methane hydrate dissociation by depressurization. *Energy Convers. Manag.* **2010**, *51*, 1883–1890. [CrossRef]
20. Ruan, X.; Song, Y.; Liang, H.; Yang, M.; Dou, B. Numerical simulation of the gas production behavior of hydrate dissociation by depressurization in hydrate-bearing porous medium. *Energy Fuels* **2012**, *26*, 1681–1694. [CrossRef]
21. Nazridoust, K.; Ahmadi, G. Computational modeling of methane hydrate dissociation in a sandstone core. *Chem. Eng. Sci.* **2007**, *62*, 6155–6177. [CrossRef]
22. Zhao, E.; Hou, J.; Liu, Y.; Ji, Y.; Liu, W.; Lu, N.; Bai, Y. Enhanced gas production by forming artificial impermeable barriers from unconfined hydrate deposits in Shenhu area of South China sea. *Energy* **2020**, *213*, 118826. [CrossRef]
23. Chen, L.; Yamada, H.; Kanda, Y.; Lacaille, G.; Shoji, E.; Okajima, J.; Komiya, A.; Maruyama, S. Numerical analysis of core-scale methane hydrate dissociation dynamics and multiphase flow in porous media. *Chem. Eng. Sci.* **2016**, *153*, 221–235. [CrossRef]
24. Wang, B.; Fan, Z.; Zhao, J.; Lv, X.; Pang, W.; Li, Q. Influence of intrinsic permeability of reservoir rocks on gas recovery from hydrate deposits via a combined depressurization and thermal stimulation approach. *Appl. Energy* **2018**, *229*, 858–871. [CrossRef]
25. Zhao, J.; Fan, Z.; Dong, H.; Yang, Z.; Song, Y. Influence of reservoir permeability on methane hydrate dissociation by depressurization. *Int. J. Heat Mass Transf.* **2016**, *103*, 265–276. [CrossRef]
26. Hardwick, J.S.; Mathias, S.A. Masuda's sandstone core hydrate dissociation experiment revisited. *Chem. Eng. Sci.* **2018**, *175*, 98–109. [CrossRef]
27. Deng, X.; Pan, S.; Zhang, J.; Wang, Z.; Jiang, Z. Numerical investigation on abnormally elevated pressure in laboratory-scale porous media caused by depressurized hydrate dissociation. *Fuel* **2020**, *271*, 117679. [CrossRef]
28. Li, Q.P.; Lv, X.; Pang, W.X.; Yao, H.Y.; Ge, Y.; Wang, J.A. Numerical Simulation of the Effect of Porous Media Permeability on the Decomposition Characteristics of Natural Gas Hydrate at the Core Scale. *Energy Fuels* **2021**, *35*, 5843–5852. [CrossRef]
29. Dai, S.; Santamarina, J.C.; Waite, W.F.; Kneafsey, T.J. Hydrate morphology: Physical properties of sands with patchy hydrate saturation. *J. Geophys. Res. Solid Earth* **2012**, *117*, B11205. [CrossRef]

30. White, M.D.; Kneafsey, T.J.; Seol, Y.; Waite, W.F.; Uchida, S.; Lin, J.S.; Myshakin, E.M.; Gai, X.; Gupta, S.; Reagan, M.T.; et al. An international code comparison study on coupled thermal, hydrologic and geomechanical processes of natural gas hydrate-bearing sediments. *Mar. Pet. Geol.* **2020**, *120*, 104566. [CrossRef]
31. Cheng, Y.; Li, L.; Yuan, Z.; Wu, L.; Mahmood, S. Finite element simulation for fluid–solid coupling effect on depressurization-induced gas production from gas hydrate reservoirs. *J. Nat. Gas Sci. Eng.* **2013**, *10*, 1–7. [CrossRef]
32. Lee, T.; Son, H.; Lee, J.; Ahn, T.; Kang, N. Geomechanically Sustainable Gas Hydrate Production Using a 3D Geological Model in the Ulleung Basin of the Korean East Sea. *Energies* **2022**, *15*, 2569. [CrossRef]
33. Liu, Z.; Lu, Y.; Cheng, J.; Han, Q.; Hu, Z.; Wang, L. Geomechanics involved in gas hydrate recovery. *Chin. J. Chem. Eng.* **2019**, *27*, 2099–2106. [CrossRef]
34. Wu, Z.; Yang, S.; Liu, W.; Li, Y. Permeability analysis of gas hydrate-bearing sand/clay mixed sediments using effective stress laws. *J. Nat. Gas Sci. Eng.* **2022**, *97*, 104376. [CrossRef]
35. Sun, X.; Li, Y.; Liu, Y.; Song, Y. The effects of compressibility of natural gas hydrate-bearing sediments on gas production using depressurization. *Energy* **2019**, *185*, 837–846. [CrossRef]
36. Jang, J.; Dai, S.; Yoneda, J.; Waite, W.F.; Stern, L.A.; Boze, L.G.; Collett, T.S.; Kumar, P. Pressure core analysis of geomechanical and fluid flow properties of seals associated with gas hydrate-bearing reservoirs in the Krishna-Godavari Basin, offshore India. *Mar. Pet. Geol.* **2019**, *108*, 537–550. [CrossRef]
37. Kimoto, S.; Oka, F.; Fushita, T.; Fujiwaki, M. A chemo-thermo-mechanically coupled numerical simulation of the subsurface ground deformations due to methane hydrate dissociation. *Comput. Geotech.* **2007**, *34*, 216–228. [CrossRef]
38. Sun, X.; Luo, H.; Soga, K. A coupled thermal–hydraulic–mechanical–chemical (THMC) model for methane hydrate bearing sediments using COMSOL Multiphysics. *J. Zhejiang Univ.-Sci. A* **2018**, *19*, 600–623. [CrossRef]
39. Sun, X.; Luo, T.; Wang, L.; Wang, H.; Song, Y.; Li, Y. Numerical simulation of gas recovery from a low-permeability hydrate reservoir by depressurization. *Appl. Energy* **2019**, *250*, 7–18. [CrossRef]
40. Cheng, W.; Lu, C.; Ning, F.; Jia, M. A coupled thermal-hydraulic-mechanical model for the kinetic dissociation of methane hydrate in a depressurizing well. *J. Pet. Sci. Eng.* **2021**, *207*, 109021. [CrossRef]
41. Wan, Y.; Wu, N.; Chen, Q.; Li, W.; Hu, G.; Huang, L.; Ouyang, W. Coupled thermal-hydrodynamic-mechanical–chemical numerical simulation for gas production from hydrate-bearing sediments based on hybrid finite volume and finite element method. *Comput. Geotech.* **2022**, *145*, 104692. [CrossRef]
42. Yasuda, S.; Masuda, T.; Yoshida, N.; Nagase, H.; Kiku, H.; Itafuji, S.; Mine, K.; Sato, K. Torsional chear and triaxial compression tests on deformation characters of sands before and after liquefaction. In Proceedings of the Fifth US-Japan Workshop on Earthquake Resistant Design of Lifeline Facilities and Countermeasures against Soil Liquefaction, Snowbird, UT, USA, 29 September 1994; pp. 249–265.
43. Masuda, Y. Modeling and experimental studies on dissociation of methane gas hydrates in Berea sandstone cores. In Proceedings of the Third International Gas Hydrate Conference, Salt Lake City, UT, USA, 18–22 July 1999.
44. Song, R.; Feng, X.; Wang, Y.; Sun, S.; Liu, J. Dissociation and transport modeling of methane hydrate in core-scale sandy sediments: A comparative study. *Energy* **2021**, *221*, 119890. [CrossRef]
45. Biot, M.A. General theory of three-dimensional consolidation. *J. Appl. Phys.* **1941**, *12*, 155–164. [CrossRef]
46. Detournay, E.; Cheng, A.H.D. Fundamentals of poroelasticity. In *Analysis and Design Methods*; Pergamon: Oxford, UK, 1993; pp. 113–171.
47. Fatt, I.; Davis, D.H. Reduction in permeability with overburden pressure. *J. Pet. Technol.* **1952**, *4*, 16-16. [CrossRef]
48. Fatt, I. The effect of overburden pressure on relative permeability. *J. Pet. Technol.* **1953**, *5*, 15–16. [CrossRef]
49. Van der Knaap, W. Nonlinear behavior of elastic porous media. *Trans. AIME* **1959**, *216*, 179–187. [CrossRef]
50. Hubbert, M.K.; Rubey, W.W. Role of fluid pressure in mechanics of overthrust faultingi. mechanics of fluid-filled porous solids and its application to overthrust faulting. *GSA Bull.* **1959**, *70*, 115–166. [CrossRef]
51. Zimmerman, R.W.; Somerton, W.H.; King, M.S. Compressibility of porous rocks. *J. Geophys. Res. Solid Earth* **1986**, *91*, 12765–12777. [CrossRef]
52. Schutjens, P.M.T.M.; Hanssen, T.H.; Hettema, M.H.H.; Merour, J.; De Bree, P.; Coremans, J.W.A.; Helliesen, G. Compaction-induced porosity/permeability reduction in sandstone reservoirs: Data and model for elasticity-dominated deformation. *SPE Reserv. Eval. Eng.* **2004**, *7*, 202–216. [CrossRef]
53. Gray, D.H.; Fatt, I. The effect of stress on permeability of sandstone cores. *Soc. Pet. Eng. J.* **1963**, *3*, 95–100. [CrossRef]
54. Haghi, A.H.; Chalaturnyk, R.; Ghobadi, H. The state of stress in SW Iran and implications for hydraulic fracturing of a naturally fractured carbonate reservoir. *Int. J. Rock Mech. Min. Sci.* **2018**, *105*, 28–43. [CrossRef]
55. McLatchie, A.S.; Hemstock, R.A.; Young, J.W. The effective compressibility of reservoir rock and its effects on permeability. *J. Pet. Technol.* **1958**, *10*, 49–51. [CrossRef]
56. Zhu, W.; Wong, T.F. The transition from brittle faulting to cataclastic flow: Permeability evolution. *J. Geophys. Res. Solid Earth* **1997**, *102*, 3027–3041. [CrossRef]